



Morphological and stoichiometric optimization of Cu₂O thin films by deposition conditions and post-growth annealing

Medina Umar^a, Milo Y. Swinkels^a, Marta De Luca^a, Claudia Fasolato^{a,b}, Lucas Moser^a, Gerard Gadea^a, Laurent Marot^a, Thilo Glatzel^{a,*}, Iliaria Zardo^{a,*}

^a Department of Physics, University of Basel, Klingelbergstrasse 82, 4056 Basel Switzerland

^b Department of Physics and Geology, Università degli Studi di Perugia, 1, 06123 Perugia, Italy

ARTICLE INFO

Keywords:

Metal oxide
Copper oxide phases
Radio frequency-magnetron sputtering
Crystallite growth
Annealing in vacuum
Contact potential difference

ABSTRACT

Thin films of copper oxide were grown by radio frequency-magnetron sputtering in an oxygen-argon environment onto silicon substrates at two different oxygen partial pressures (15% and 23%). Post deposition annealing in vacuum environment was conducted on the films at different temperatures (between 250 °C and 550 °C). We investigated the thin films by Scanning Electron Microscopy, Energy Dispersive X-ray, X-ray diffraction, Raman spectroscopy, Atomic Force Microscopy and Kelvin Probe Force Microscopy. These studies show that post-growth annealing in vacuum results in thin films with different morphological and stoichiometric properties. Furthermore, the oxygen partial pressure conditions during deposition have an impact over the obtained oxide phases: high oxygen partial pressure leads to the formation of two different oxide phases, i.e. CuO and Cu₂O, while low oxygen partial pressure leads to the formation of Cu₂O thin films. Notably, we also uncovered a parasitic crystallite growth as a result of aging on the pristine and low-temperature annealed samples, and we found out that high temperature annealing prevents this kind of aging.

1. Introduction

Metal Oxides (MOs) form an important group of functional materials with diverse structural, electronic, magnetic, and optical properties and, as semiconductors, are promising materials for photovoltaic applications. Many MOs are abundant, non-toxic, and chemically stable, thus interesting materials for further research and development [1–4]. MOs are already widely used as active or passive components in a broad range of available applications e.g. as active channel layer in transistors [5,6], transparent conducting front electrodes [7], all-oxide photovoltaic cells [8,9], Active Matrix Organic Light Emitting Diode displays [10], hetero-interfaces for solar cell applications [11,12], gas sensors [13], and photocatalytic activity studies [14,15]. Theoretical calculations have predicted an efficiency of oxide-based solar cells of over 20% [16, 17].

Copper oxide is an MO with three possible oxide phases, namely Cu₂O, CuO and Cu₄O₃. The oxide growth kinetic of these three oxides depends largely on the oxygen pressure, temperature, and speed of deposition rate; therefore, a very slim window of deposition parameters for obtaining a specific oxide phase exists, and the distinguishing factors

are the growth parameters. From the equilibrium phase diagram, Cu₂O (Cu⁺) and CuO (Cu²⁺) are the stable phases. The preferred phase for its potential for photovoltaic application in dye sensitized wide band gap devices is Cu₂O (cuprous oxide) with a simple cubic structure and space group O_h^4 with two molecules per unit cell; it is a p-type direct band gap II-VI semiconductor [18–20] with reported direct band gap energy value of 2.17 eV and optical band gap energy values of 2.32 to 2.62 eV [21–24]. CuO (cupric oxide) has a monoclinic structure with band gap energy values of 1.21–1.51 eV [25,26], while Cu₄O₃, a tetragonal crystal system for which there are very few studies, is called paramelaconite, and has a band gap of about 1.34 eV [22,27].

Several deposition techniques have been applied and reported for cuprous oxide, such as plasma evaporation [28], chemical deposition [23,29–32], oxidation [33], electrochemical deposition [34,35], remote plasma deposition [36], and magnetron sputtering techniques [37–41]. Depositions were performed onto different substrates such as glass, quartz, fibre glass, substrates [27,41–43], soda-lime glass [44], silicon wafers [45–47], stainless steel substrates [48], co-fired ceramics substrates [49], plastic and polyethylene terephthalate substrates [10,50]. The resulting morphology and grain size largely depend on the

* Corresponding authors.

E-mail addresses: thilo.glatzel@unibas.ch (T. Glatzel), iliana.zardo@unibas.ch (I. Zardo).

<https://doi.org/10.1016/j.tsf.2021.138763>

Received 28 June 2020; Received in revised form 21 May 2021; Accepted 24 May 2021

Available online 31 May 2021

0040-6090/© 2021 The Author(s).

Published by Elsevier B.V. This is an open access article under the CC BY-NC-ND license

(<http://creativecommons.org/licenses/by-nc-nd/4.0/>).

Table 1

Deposition parameters for the two series of thin films in the RF-magnetron sputtering machine and resulting thickness.

Deposition at low oxygen ratio	Deposition at high oxygen ratio
Excitation: RF = 13.56 MHz	Excitation: RF = 13.56 MHz
Power = 100 W	Power = 100 W
Partial pressure of O ₂ = 1.7 × 10 ⁻¹ Pa → 15%	Partial pressure of O ₂ = 2.6 × 10 ⁻¹ Pa → 23%
Partial pressure of Ar = 9.6 × 10 ⁻¹ Pa → 85%	Partial pressure of Ar = 8.8 × 10 ⁻¹ Pa → 77%
Total pressure = 1.09 Pa	Total pressure = 1.09 Pa
Deposition time = 130 s	Deposition time = 130 s
Thin film thickness ~ 150 nm	Thin film thickness ~ 330 nm

technique used for the deposition process; the common morphologies are tetragonal [44,48], octahedral [23], and cubic [43,45,51]. There are extremely few studies on the stability and aging of copper oxides [52, 53].

In this paper, we synthesize copper oxide thin films from sputtering of pure copper targets at room temperature using radio frequency (RF)-magnetron sputtering technique. Moreover, we conduct post-deposition annealing in vacuum on the grown films at different temperatures. Annealing in vacuum has been employed in a variety of studies to obtain desirable film properties. For copper oxides, the majority of these studies was performed under an oxygen and nitrogen atmosphere [54,55]. As these gases could have further reactions with the films atoms, in this work we perform the annealing in near vacuum conditions. This has the additional potential benefit of reducing the oxygen content of the film helping to create the desired Cu₂O, which is otherwise difficult to obtain directly from growth. Moreover, also its band gap may be tuned by enhancing the grain sizes and the crystallinity of thin films via annealing [55,56].

We systematically investigate the obtained films via Scanning Electron Microscopy (SEM), Energy-dispersive X-ray spectroscopy (EDX), X-ray diffraction (XRD), Raman spectroscopy, Atomic Force Microscopy (AFM), and Kelvin Probe Force Microscopy (KPFM). We show that performing annealing in vacuum allows to improve the properties of the films, such as grain size and surface-to-volume ratio, while also improving the stoichiometry. This work constitutes an unprecedented complete study of the temperature dependent effects of vacuum annealing on copper oxide films, both grown as nominally CuO as well as nominally Cu₂O.

2. Experimental details

2.1. Film deposition

The deposition of copper oxide films was performed in a high vacuum chamber pumped with base pressure of about 2 × 10⁻⁴ Pa [57]. Copper oxide films were grown onto ultrasonically pre-cleaned silicon wafers with the [100] orientation using reactive magnetron sputtering. The copper target (99.9% purity, oxygen-free high thermal conductivity) has a diameter of 2 cm. Argon (99.9999%) and oxygen (99.9995%), introduced through a mass flow controller, were used as sputter gas with the flow rate being fixed at 6.0 (Ar): 4.0 (O₂) sccm and 6.6 (Ar): 2.5 (O₂) sccm respectively for the high and low oxygen partial pressure depositions. The estimated target-to-substrate distance was 7 cm, and the deposition process carried out at room temperature at fixed RF electrical power of 100 W (at 13.56 MHz) applied to the target. We used two set of parameters (see Table 1 for the deposition environments description), resulting in two different samples: one with a low partial pressure of 15% and one with a high partial pressure of 23%. The post-deposition treatment, i.e. annealing in near vacuum conditions, was conducted on samples cleaved after deposition from the original sample, such that any difference that would arise in the properties would come from the

annealing at different temperatures and not from slightly different deposition parameters. Before annealing, the chamber was flushed in argon to avoid any remaining oxygen and then pumped down to approximately 500 Pa. The annealing temperatures were 250, 350, 450, 500 and 550 °C, the ramping time was 300 s, the samples annealing time was one hour each.

The cross sections of the films obtained via SEM at a tilt angle of 90° are shown in Fig. A.1 in the Appendix A. Fig. A.2 displays the measured thickness of all thin films. We found a film thicknesses of ~150 nm for the pristine 15% O₂ and ~330 nm for the pristine 23% O₂ partial pressures. Clearly, the overall film thickness is only marginally affected by the annealing temperature. The larger thickness for the 23% sample with respect to the 15% one likely comes from the different positioning of the samples on our sample holder during the deposition, which can lead to different deposition rates. Our 58 mm diameter sample holder is comparable to the sputtering plume in size and hence we have a maximum deposition rate at the center, with a radial decay following a Gaussian profile. The 23% sample was placed closer to the holder's center and hence the deposition rate – and thus the thickness for an equal process time – was higher. Further investigations are ongoing and go beyond the scope of this work. We stress that a different thickness does not affect sample' properties, but only the visibility of substrate peaks in some characterization techniques, as it will be discussed.

2.2. Thin films characterization

The surface morphology of the prepared films was examined using SEM operated at 5 kV, and micrographs at different magnifications were obtained. The SEM was performed with the Leo Supra 35 microscope by ZEISS. Energy and Dispersive X-ray (EDX) scans were performed using EDAX32\Genesis at accelerating voltage of 10 kV on both the pristine and the samples annealed at 500 °C to detect the thin films' elemental composition. The analysis probing depth is 1 μm on average (the effective value depends on the material properties, including density). The chemical composition and the structural properties of the grown thin films were studied by means of XRD and Raman spectroscopy. XRD patterns were recorded using a SIEMENS D5000 instrument with Cu Kα radiation (λ = 1.5418 Å, 40 kV and 30 mA) at a grazing incidence of 5°. Grazing incidence probes the crystallography film surface within a few nm. A graphite secondary monochromator (no filter) was used and a width of 1° for the primary and secondary divergence slits was employed. All XRD patterns were acquired with scan steps of 0.02° and with 8 s of acquisition time. The Stokes Raman spectra were acquired at room temperature, the excitation wavelength was 532 nm, the power density was fixed to 250 kW/cm² to avoid laser-induced sample modification/damage, and the laser beam was focused on the sample surface using a 100x objective, resulting in a spot size of about 0.6 μm. The scattered light was collected in backscattering geometry and analysed using a spectrometer with a 600 grooves/mm grating. AFM measurements were carried out inside a glove box (labmaster 130, mBraun) under a dry nitrogen atmosphere (< 0.1 ppm H₂O and O₂) with a commercial microscope (FlexAFM, Nanosurf) in standard tapping mode at the first cantilever resonance. The electrical analysis was conducted via KPFM employing the use of the single pass mode to capture both the topography and the contact potential difference (CPD) simultaneously with amplitude modulation [58,59]. An external lock-in amplifier (HF2, Zurich Instruments) was employed to excite, detect and compensate the electrostatic forces at the second resonance of the cantilever [60]. The data acquisition was performed using a PtIr coated cantilever (PPP-NCLPT, Nanosensors).

3. Results and discussion

3.1. Morphology and compositional analysis

The grown thin films were analysed via SEM to study the evolution of

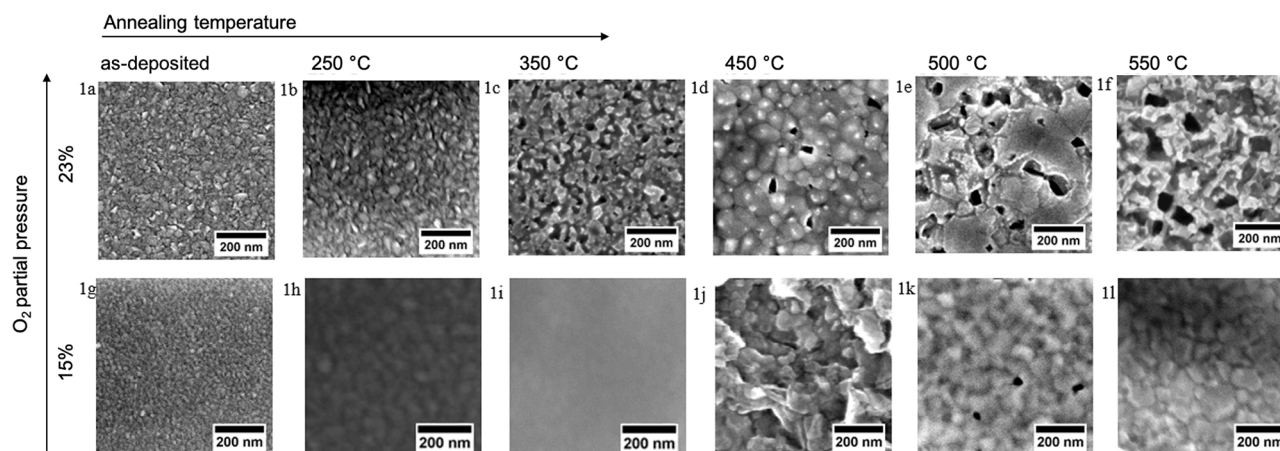


Fig. 1. SEM surface morphology of sputtered thin films on Si substrates deposited at 15% (bottom panels) and 23% (top panels) O_2 partial pressure. Annealing temperature increases from left to right.

Table 2

EDX results for Cu-O elements in as-deposited and annealed at 500 °C thin films deposited at 15% and 23% O_2 partial pressures extracted from the EDX data in Fig. B.1 in Appendix B.

Samples	Annealing temperatures (°C)	Element	Weight %	Atomic %
15% O_2 at deposition	not annealed	O	15	41
		Cu	85	59
	500	O	14	40
		Cu	86	60
23% O_2 at deposition	not annealed	O	23	55
		Cu	77	45
	500	O	20	49
		Cu	80	51

the surface morphology with annealing temperature. The obtained images of the as-deposited and annealed films formed with 23% or 15% O_2 partial pressure are presented in Fig. 1a-f and 1g-l, respectively. The as-deposited films in Figs. 1a and 1g show densely packed grains that are homogeneously distributed and very similar to the observation of the nanoporous CuO material synthesized by microwave-assisted synthesis [22,61]. The pattern and shape of the annealed thin films evolve greatly with the temperature increase, as visible in panels b-f and h-l: besides the change in the morphology of the grains, which become bigger and less homogeneous, we also notice black spots on the annealed samples that are conspicuous in Figs. 1c, 1e, 1f and 1j, showing some void-like features or micro cracks, likely as a result of the thermal expansion coefficient difference between the films and the substrate [62]. The increase in nucleation, and in the active surface area, can be attributed to atomic diffusion. We observe that although films with both oxygen ratios show a change in morphology caused by the annealing, the 23% O_2 partial pressure sample shows more agglomeration of grains since the oxygen rate is higher. The 15% O_2 partial pressure samples at higher annealing temperatures of 500 and 550 °C in Figs. 1k and 1j show well defined and clear edge crystallites indicating full crystallization.

The EDX characterization, aimed at elemental identification and composition analysis, was conducted on both the pristine and the annealed films at 500 °C, for both O_2 partial pressures. The EDX spectra and results, displayed in Fig. B.1 in the Appendix B and in Table 2, respectively, show that in the sample deposited at high partial pressure the oxygen percentage decreases in both the elemental weight and the atomic percentage due to annealing, suggesting an annealing-mediated

change in the relative copper and oxygen contents possibly related to phase change, which we have further investigated by XRD and Raman in Section 3.2. De-oxidation of materials when subjected to vacuum annealing was reported previously, for example in metals (see, e.g., [63]) and semiconductors (e.g. [64]). Usually these studies are performed to get rid of unwanted native oxide, while in our work we find that vacuum annealing can also be employed to change the stoichiometry of the film. Since the native oxide is often only on the surface, we perform several bulk-type analyses (e.g. Raman) and show that the stoichiometry is changed throughout the film.

3.2. Structural properties

The structural analysis was performed using XRD in the scanning Bragg angle 2θ from 20° to 90°. The Cu_2O phase belongs to the space group $Pn\bar{3}m$ or O_h^4 , documented in the Inorganic Crystal Structure Database (ICSD) pattern 01-077-0199, while the CuO has the space group $C2/c$ (ICSD pattern 00-045-0937). Fig. 2 presents the XRD results. The thin films sputtered at 15% O_2 partial pressure (see panel 2a and its magnification below it) have patterns indexed to planes of the Cu_2O phase, namely the reflections at 29.56° (110), 36.18° (111) and 42.43° (200). In the 350 °C sample, the plane at 29.04° (110) is attributed to the Cu_2O . The data indicate a phase transition at 450 °C, where both oxides coexist. Indeed, the diffraction peaks at 35.70° ($\bar{1}11$) [24] and at 38.86° (200) are attributed to CuO. At 500 °C and 550 °C we notice the disappearance of the CuO peaks, while all the Cu_2O peaks stay.

The pristine films sputtered at 23% O_2 partial pressure (panel 2b in Fig. 2 and its magnification) show diffraction peaks of CuO at 35.43° ($\bar{1}11$) and at 38.54° ($\bar{1}11$) [65] at all annealing temperatures. Moreover, at 350 °C a peak at 36.29° (111) belonging to Cu_2O arises and it stays up to 550 °C. The peak at 38.86° is indexed to the (200) plane of CuO. The 450 °C has a peak at 42.89° (200) from Cu_2O . Figuredo [24] and Nair [60] revealed in their temperature studies that at temperatures greater than 350 °C Cu_2O could reverse to CuO, while in our study we observe both this and the reverse trend. The observation of the reverse trend could arise from the fact that in those studies annealing was performed in air, while in our study it was performed in vacuum. The annealing-driven reduction process leads to the formation of stable Cu_2O . In our work, depending on the used oxygen pressure, we observe Cu_2O reversing to CuO at 450 °C (for the low O_2 partial pressure deposited samples) and CuO transforming to Cu_2O at 350 °C (for the high O_2 partial pressure deposited samples), the latter being similar to ref. [65]. We stress that we did not observe any peak coming from the Si (100) substrate, as expected for a grazing incidence XRD experiment with the incidence angle of 5° chosen in this work.

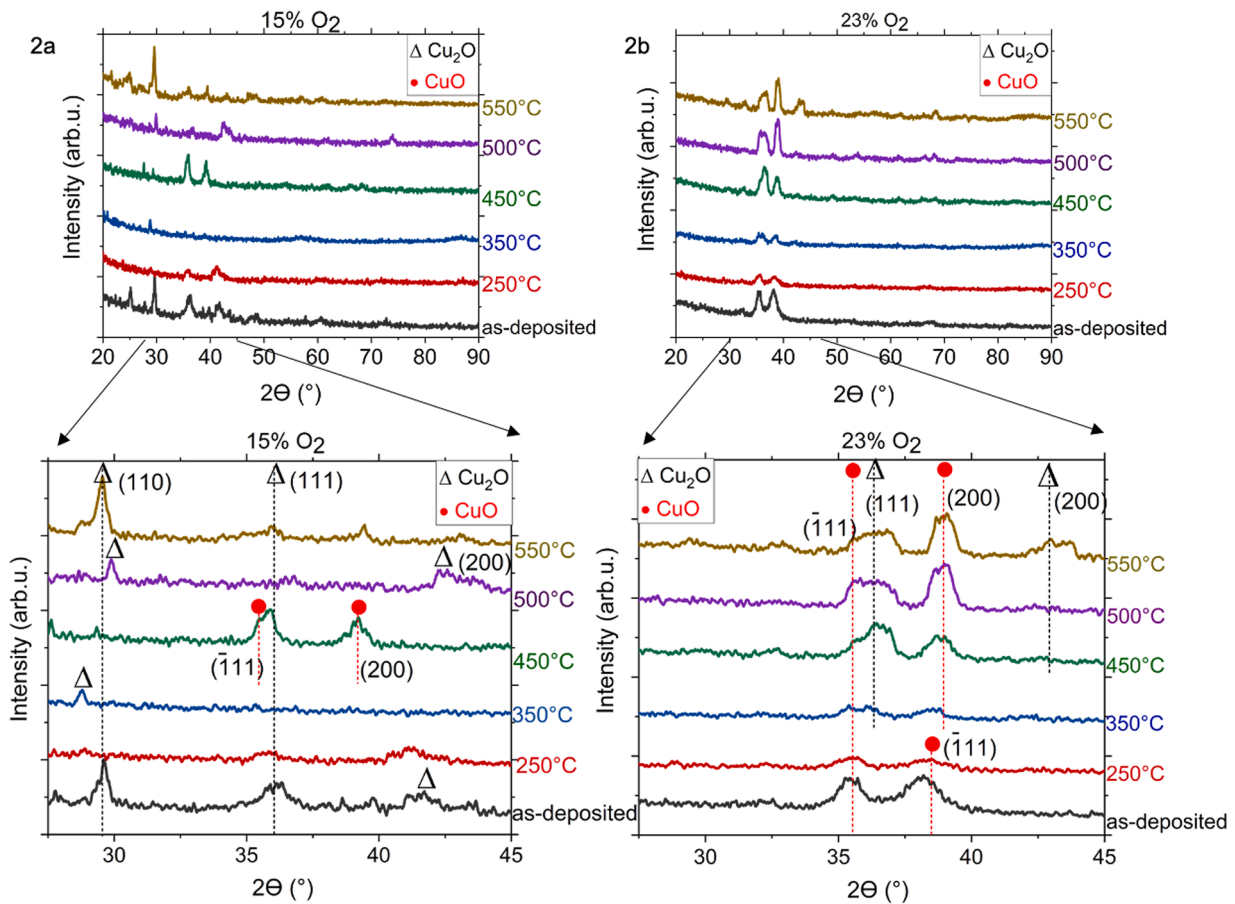


Fig. 2. Stacked XRD patterns of thin films prepared on Si substrates by RF-magnetron sputtering at 15% (panel 2a) and 23% (panel 2b) O_2 partial pressure. The bottom panels offer a magnified view of the top panels, in the region 27–45°. Triangles and circles indicate peaks attributed to Cu_2O or CuO , respectively, and the dashed lines highlight their evolution. Annealing temperature of each sample is indicated on the right side.

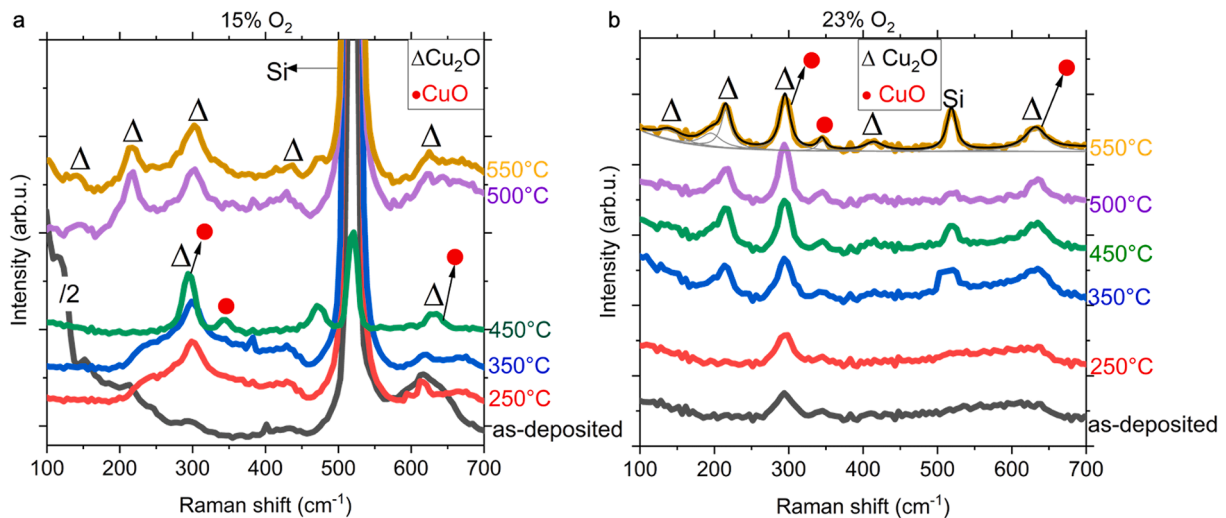


Fig. 3. Stacked Raman spectra of thin films prepared on Si at 15% (panel 3a) and 23% (panel 3b) O_2 partial pressure. Annealing temperature of each sample is indicated on the right side. In panel 3a, the as-deposited sample's spectrum is halved (see the division by 2). Peaks attributed to Cu_2O or CuO are indicated by triangles and circles, respectively, and the Si substrate peak at $\sim 521\text{ cm}^{-1}$ is indicated by 'Si'. In the spectrum of the 550 °C sample in panel 3b we show the fitting procedure: grey thin lines indicate the Lorentzian components, and the black thin line is the cumulative result.

To further elucidate the structural composition of the thin films and its dependence on annealing temperature, we performed Raman spectroscopy studies on all films. Fig. 3 shows the Raman spectra of the as-deposited and annealed thin films for both sputtering processes at

15% and 23% O_2 (panels 3a and 3b, respectively). We performed a careful quantitative analysis of the collected spectra. As an example of the deconvolution procedure, we display the fitting of the whole spectrum of the sample deposited at 23% O_2 and annealed at 550 °C in

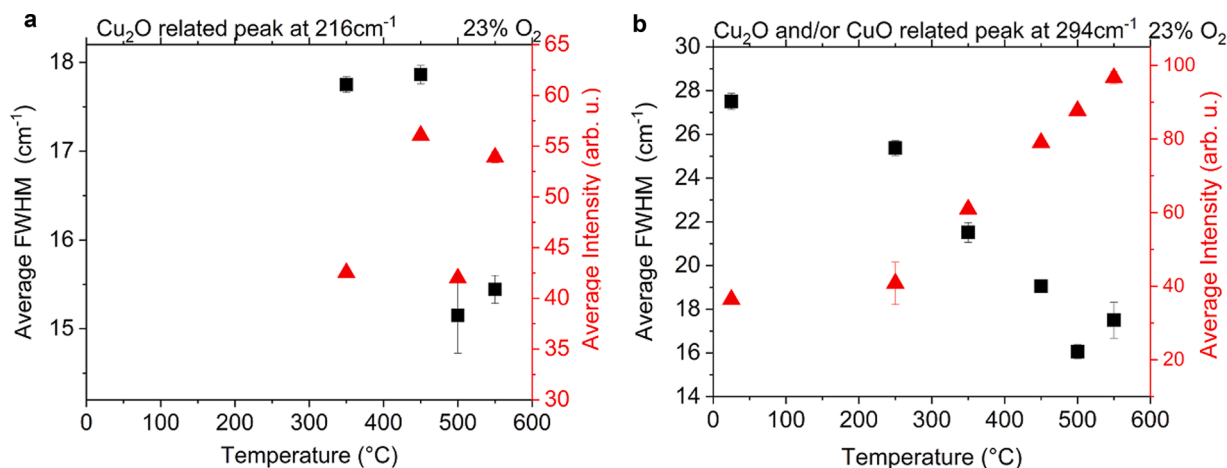


Fig. 4. Intensity (red triangles) and FWHM (black squares) relative to the 216 cm^{-1} phonon mode (panel 4a) and to the 294 cm^{-1} mode (panel 4b) as extracted from the fits of the Raman spectra of the 23% O_2 sample in Fig. 3b. The spectra were obtained in two different locations on the samples at a distance of $\sim 50\ \mu\text{m}$, and the data in Fig. 4 represent the average of the results, with error bars coming from the semi-dispersion.

Fig. 3b (see grey and black thin lines), from which we derived the full width at half maximum (FWHM), the average intensity, and mean frequency of each peak. The FWHM and the average intensity are plotted in Fig. 4 for selected phonon modes of the 23% O_2 sample. In all the spectra shown in Fig. 3, the peak at 521 cm^{-1} belongs to the optical F_{2g} phonon mode of the Si substrate. In the thinner films, namely, those deposited at 15% oxygen partial pressure, the Si substrate signal is very intense in all the spectra, as expected due to the small film thickness. In the 15% O_2 sputtered thin films annealed at high temperatures, $500\text{ }^\circ\text{C}$ and $550\text{ }^\circ\text{C}$, we observe a peak at 145 cm^{-1} , which can be assigned to phonons of symmetry F_{1u} of Cu_2O [45] [65]. The next peak that we observe is at 214 cm^{-1} . It has very low-intensity in the as-deposited thin film and in the annealed ones at 250, 350, and $450\text{ }^\circ\text{C}$ [66]. This peak shifts to 216 cm^{-1} and largely grows in intensity for annealing temperatures higher than $500\text{ }^\circ\text{C}$. It corresponds to the second order Raman-allowed mode $2\Gamma_{12}$ of Cu_2O [45] [67]. The small peak at 436 cm^{-1} in the $550\text{ }^\circ\text{C}$ annealed sample can be ascribed to the combination of four phonon modes, $3\Gamma_{22} + \Gamma_{25}$, of Cu_2O [68–70]. The broad asymmetric peak at 428 cm^{-1} visible in all the samples (with the exception of the $450\text{ }^\circ\text{C}$ sample, in which for a reason that we are still investigating the modes coming from the substrate are not very visible) is ascribed to the acoustic modes of the Si substrate. The broad peak centred at 302 cm^{-1} and visible at temperatures 250, 350, 500 and $550\text{ }^\circ\text{C}$ is a second order mode of the silicon substrate. That peak is clearly distinguishable (due to its spectral shape and frequency) from the prominent peak at 294 cm^{-1} , visible in the thin film annealed at $450\text{ }^\circ\text{C}$, attributed to a second order overtone mode with A_{2u} symmetry belonging to Cu_2O [45]. We notice that this peak would also be compatible with the A_g mode of CuO when it is strained or nanostructured [69]. As indicated by the symbols in the figure, we have considered also this possible assignment because of the presence of grains in our thin films. The sample at $450\text{ }^\circ\text{C}$ has a weak peak at 344 cm^{-1} , which may be attributed to a B_g mode of CuO [46,71]. The peak at 470 cm^{-1} disappears at $500\text{ }^\circ\text{C}$ and reappears weaker at $550\text{ }^\circ\text{C}$. The peak at about 635 cm^{-1} , whose frequency agrees with the infrared-allowed transverse optical mode of Cu_2O with symmetry Γ_{15} , can be observed in a Raman scattering experiment as a result of selection-rules violation mechanisms [46,70,72]. We observe that this peak may be compatible with B_g mode of CuO and is interpreted as Raman-allowed optical phonon mode of CuO [73]. The samples annealed at 250 and 350, 500 and $550\text{ }^\circ\text{C}$ show instead a peak at 624 cm^{-1} attributed to Cu_2O [74]. Similarly to the XRD data, the Raman data point to a phase transition occurring at $450\text{ }^\circ\text{C}$ that makes this a crucial temperature for the deposition process performed at 15% O_2 . Our results show that at low (15%) reactive deposition gas Cu_2O can be obtained

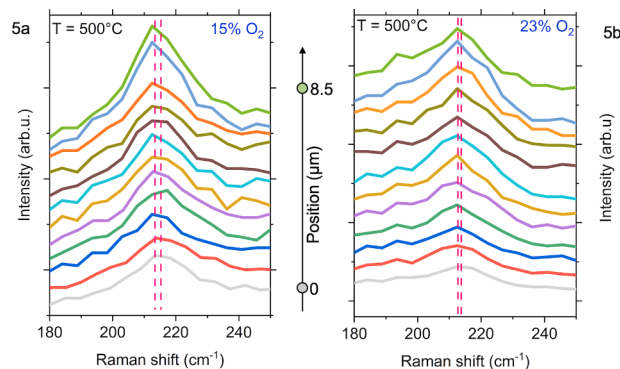


Fig. 5. Stacked Raman spectra magnified in the frequency region of the Cu_2O mode at 216 cm^{-1} acquired on twelve different positions of the samples with 15% (panel 5a) and 23% (panel 5b) O_2 partial pressure annealed at $500\text{ }^\circ\text{C}$. Data were obtained by mapping the samples over an area of $6 \times 6\ \mu\text{m}^2$ with steps of $0.5\ \mu\text{m}$. Dashed lines mark variation in central frequency of the mode, which for a) is $\sim 2\text{ cm}^{-1}$ and for b) is $\sim 1.2\text{ cm}^{-1}$. Fluctuations in the intensity can be attributed to slightly different focusing conditions.

and this is the case also upon annealing at high temperature.

We now turn our attention to the thin films sputtered at 23% oxygen partial pressure (Fig. 3b). Here, the increased thickness of the film screens the contribution of the Si substrate. This is expected for films made by highly absorptive materials, as copper oxides [21]. The as-grown film and the one annealed at $250\text{ }^\circ\text{C}$ contain both oxide phases of CuO and Cu_2O . Indeed, the spectra of these samples display an intense peak at 294 cm^{-1} attributed to Cu_2O (and possibly CuO as described before) [45,75]. The broad peak at 635 cm^{-1} is interpreted as discussed above [46,70,73]. The moderate peak at 344 cm^{-1} is CuO -related [46, 71]. The low intensity peak at 145 cm^{-1} is assigned to Cu_2O as discussed above [45,65]. At $350\text{ }^\circ\text{C}$, there is a phase transition associated to oxygen diffusion. This is evident in the extra Cu_2O signature peaks at 216 cm^{-1} and 416 cm^{-1} (see, e.g., the appearance of the 216 cm^{-1} mode at $350\text{ }^\circ\text{C}$ in Fig. 4a), as well as in the increase in intensity of the already present peaks at 294 cm^{-1} and at 635 cm^{-1} , which become narrower and more intense. The intensity of the 294 cm^{-1} mode increases even more for the subsequent annealing temperature of 450, 500 and $550\text{ }^\circ\text{C}$ (see its intensity as a function of annealing temperature in Fig. 4b). While its frequency stays quite constant with temperature (it varies about 1 cm^{-1} , namely less than the spectral resolution), its intensity starts to increase at $350\text{ }^\circ\text{C}$ due to the already discussed phase transition.

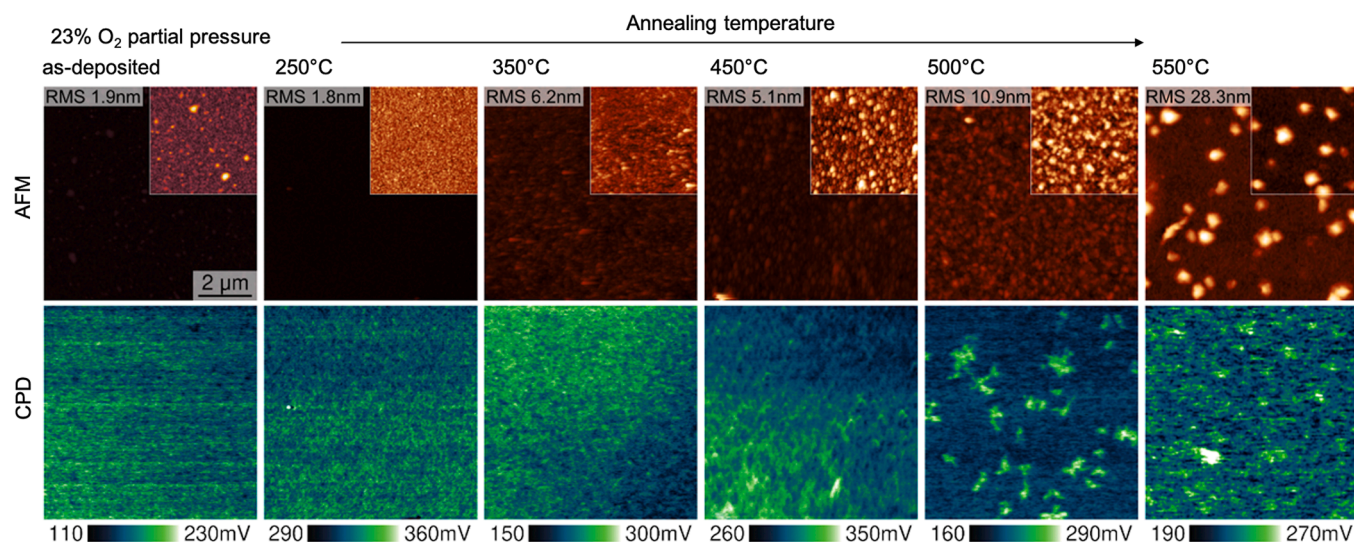


Fig. 6. AFM topography (top panels) and CPD (bottom panels) of thin films sputtered on Si substrates at 23% O₂ partial pressure and annealed at different temperatures. The scanned area is 8 × 8 μm². The height scale bar was adjusted to get Δz = 200 nm for the top panels, while the insets show a 4 × 4 μm² region with the optimal height range. The AFM images show an increase in the RMS roughness as the temperature increases.

Furthermore, its FWHM, plotted in Fig. 4b, decreases, which points to an improved crystal quality for higher annealing temperatures. Conclusively, the correlation between XRD and Raman data shows that in the samples deposited with high oxygen ratio both oxide phases co-exist and that higher oxygen pressure at deposition favours CuO, while the annealing process in vacuum partially converts CuO to Cu₂O.

We investigated the homogeneity of the films by performing spatially resolved Raman measurements over several samples. In Fig. 5 we show the results on two representative samples. We plot the Raman spectra magnified in the frequency region of the mode at 216 cm⁻¹ measured on twelve different points, spaced from each other about 0.8 μm, of the samples annealed at 500 °C for both 15% O₂ (panel 5a) and 23% O₂ (panel 5b) samples. The fluctuations in the frequency are small, lower than the spectral resolution, which points to a good homogeneity of the samples (at least on a scale larger than the laser spot) in this region (6 × 6 μm²). The homogeneity over larger distances was also confirmed (indeed, Raman spectra were obtained in two different locations on the samples at a distance of ~50 μm, and the data in Fig. 4 represent the average of the results, with error bars coming from the semi-dispersion).

3.3. Topographical studies

KPFM in tapping mode and AFM were conducted on the samples grown at 23% oxygen to obtain the topography and their CPDs, respectively. The scanned area was 8 × 8 μm² and the CPD was measured from ~110 mV to ~360 mV. In Fig. 6 we show AFM images in the top panels and their corresponding CPDs in the bottom panels. The height scale of all topography images was set to 0–200 nm. The insets in the AFM images display a 4 × 4 μm² section of the original images with the optimal height scale. We observe an increase of grains sizes as the temperature increases, which is consistent with our SEM results. The Root Mean Square (RMS) surface roughness deduced from the AFM topography images for increasing annealing temperature are: 1.9 nm, 1.8 nm, 6.2 nm, 5.1 nm, 10.9 nm and 28.3 nm.

In the bottom panels, the CPD measurements show a nearly homogeneous distribution up to an annealing temperature of 450 °C. Only above this temperature, we found regions with higher and lower CPD values correlated with higher and lower work functions, respectively. We suspect that these areas represent the co-existence of CuO and Cu₂O crystals, since EDX, XRD, and Raman all pointed to the co-existence of these two phases at 23% oxygen partial pressure for these annealing temperatures. Generally, it is expected for Cu₂O to have a lower work

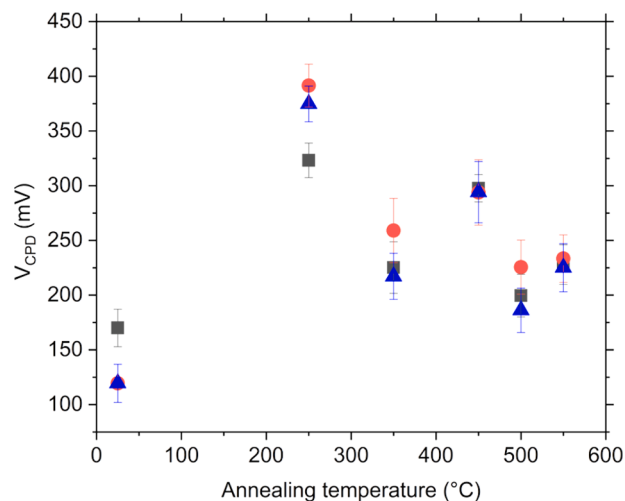


Fig. 7. CPD values extracted at three different positions on each sample. The black squares, red circles and the blue triangles represent the different positions on the sample surfaces. The error bars come from the variations in measured values for the different positions of the thin films.

function than CuO ($\Phi[\text{Cu}_2\text{O}] = 4.84$ eV and $\Phi[\text{CuO}] = 5.32$ eV [76]) which, however, depends also on crystallinity and doping concentration. This allows us to correlate the bright areas with remaining CuO segregating at 500 °C and vanishing for higher temperatures. The overall values of the work function would only be available for a calibrated tip [77]. AFM data of the samples with 15% oxygen are displayed and described in Fig. C.1 in Appendix C.

CPD values have been obtained at three different positions on each sample for all annealing temperatures, as shown in Fig. 7. This statistics proves that tip changes or sample inhomogeneity's are influencing only marginally the following conclusions. We observe an increase in the sample work function (measured as contact potential difference) of about 200 mV as temperature increases from room temperature to 250 °C. This increase is probably due to the cleaning (reorganization of the surface due to annealing in vacuum) of the CuO surface. Further increase of the temperature shows an overall decrease of the work function most probably due to the increasing formation of Cu₂O. There was a time lag between this investigation and the deposition and

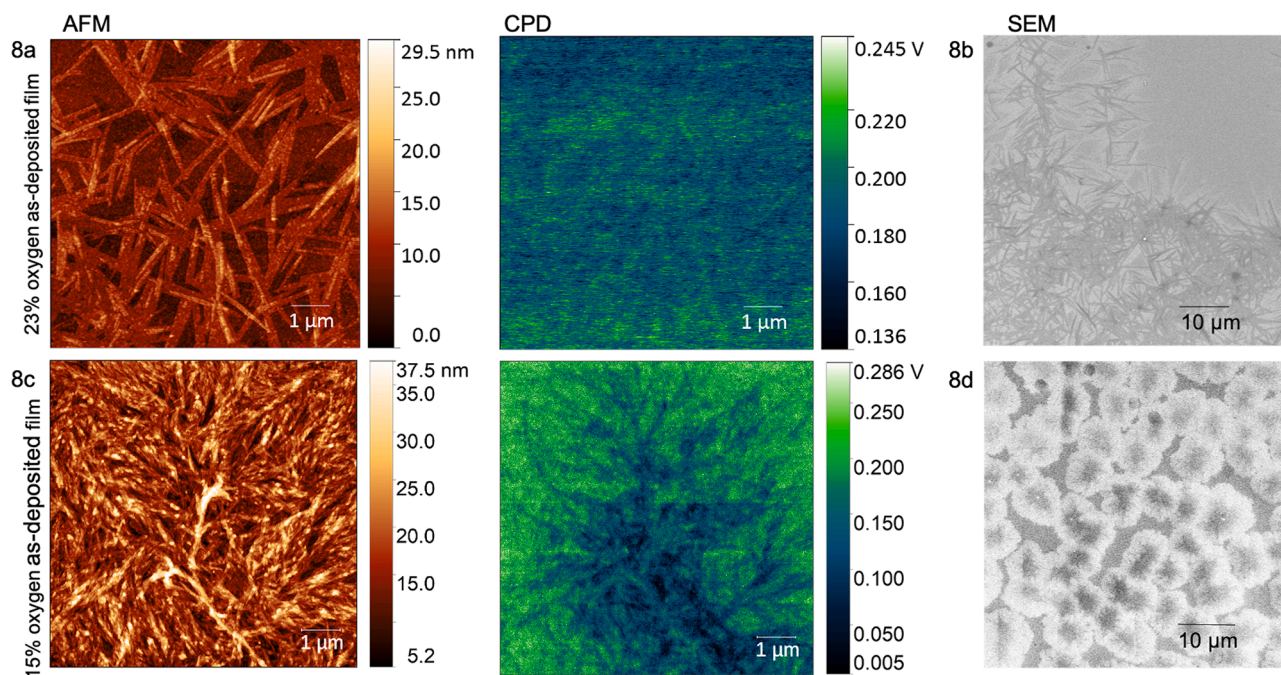


Fig. 8. AFM, CPD and SEM images of pristine films deposited at 23% O₂ (top panels or 8a and 8b) and 15% O₂ (bottom panels or 8c and 8d) showing crystallites growth. Top panels correspond to 21 months aging period and bottom panels to 15 months aging period. Samples were stored at room conditions.

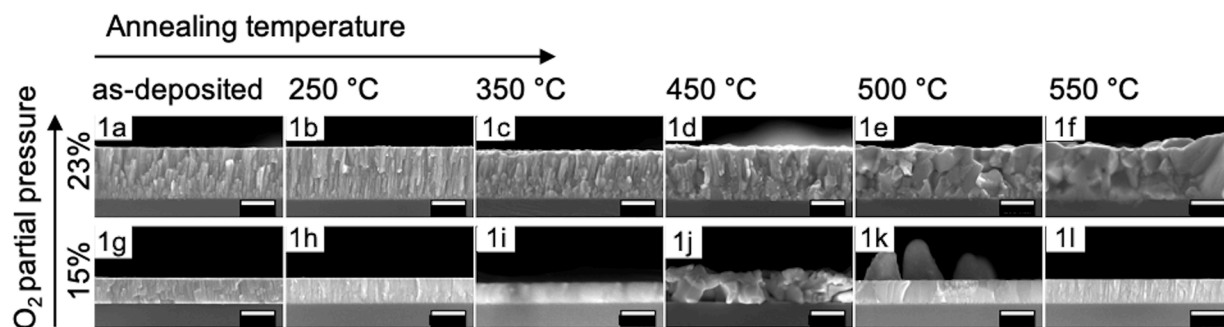


Fig. A.1. Cross-section SEM images of the thin films sputtered on Si substrates deposited at 23% (top panels, 1a-1f) and 15% (bottom panels, 1g-1l) O₂ partial pressure and annealed at the indicated temperatures. Scale bars are 200 nm.

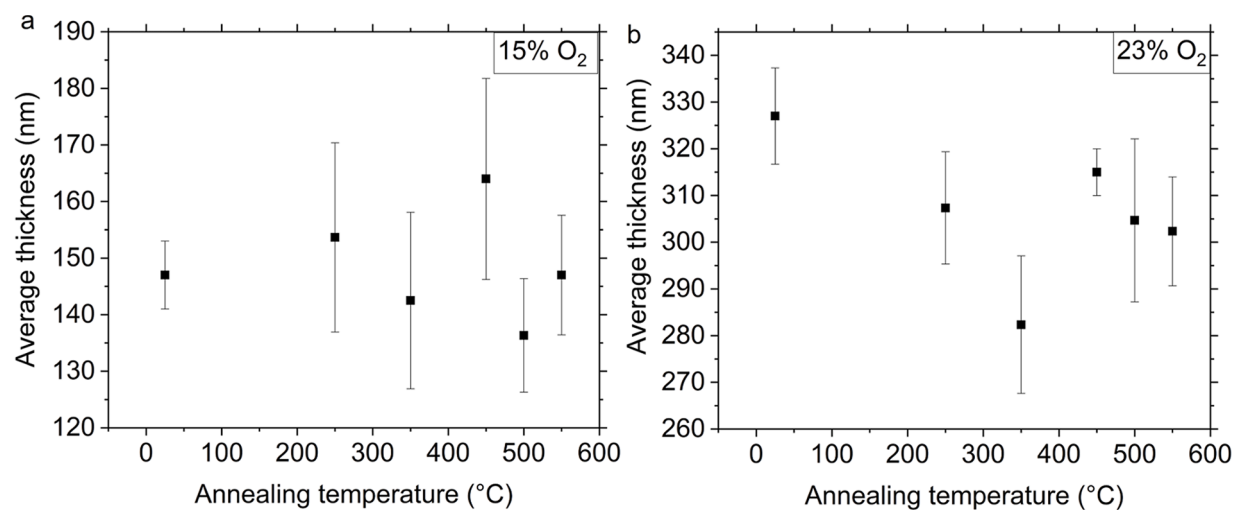


Fig. A.2. Average thickness of thin films deposited at 15% (panel a) and 23% (panel b) O₂ partial pressure and annealed at different temperatures. Thicknesses result from the cross section SEM images in Fig. A.1. Each average value comes from measurements on three different points of each sample.

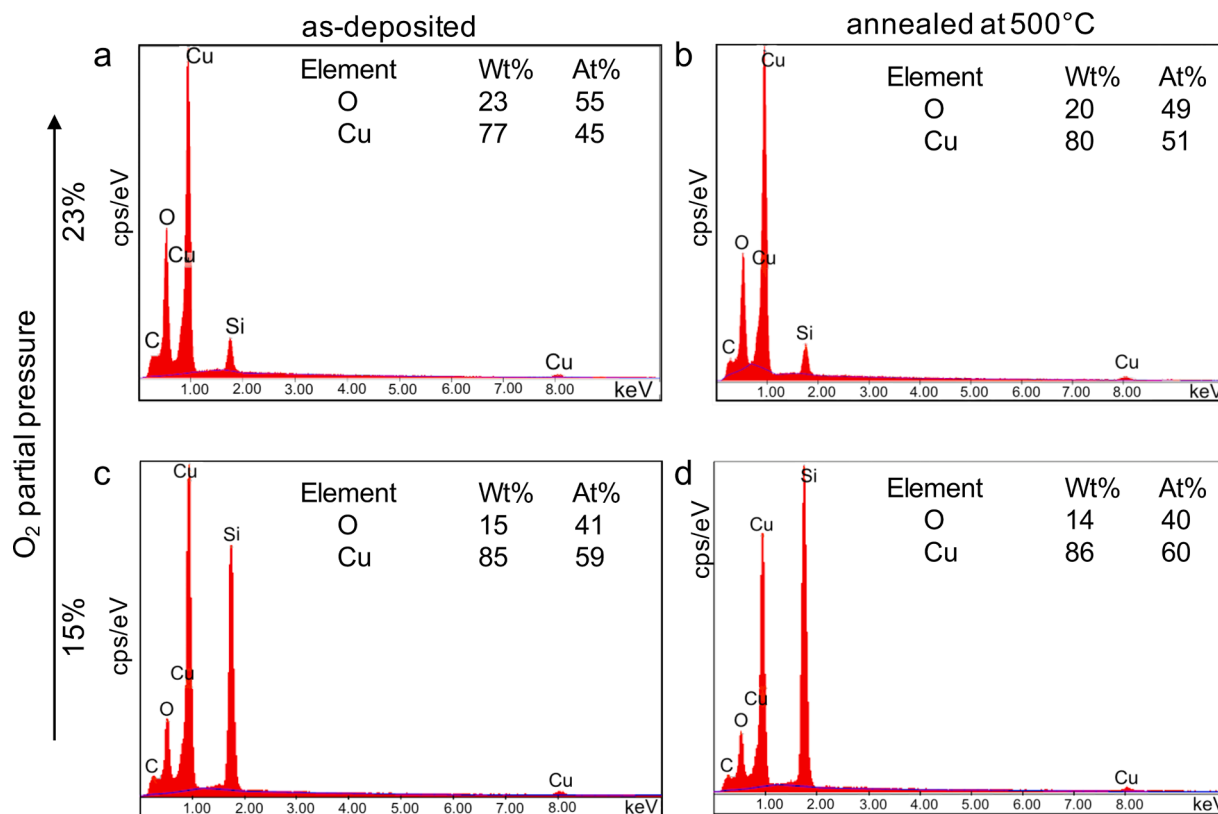


Fig. B.1. EDX spectra of as-deposited and annealed at 500°C thin films deposited at 23% (a,b panels) and at 15% (c,d) O₂ partial pressure. The data were acquired in an area of 1 × 1 μm². The signal coming from the Si substrate is evident, and it is higher in the thinner films (15% partial pressure).

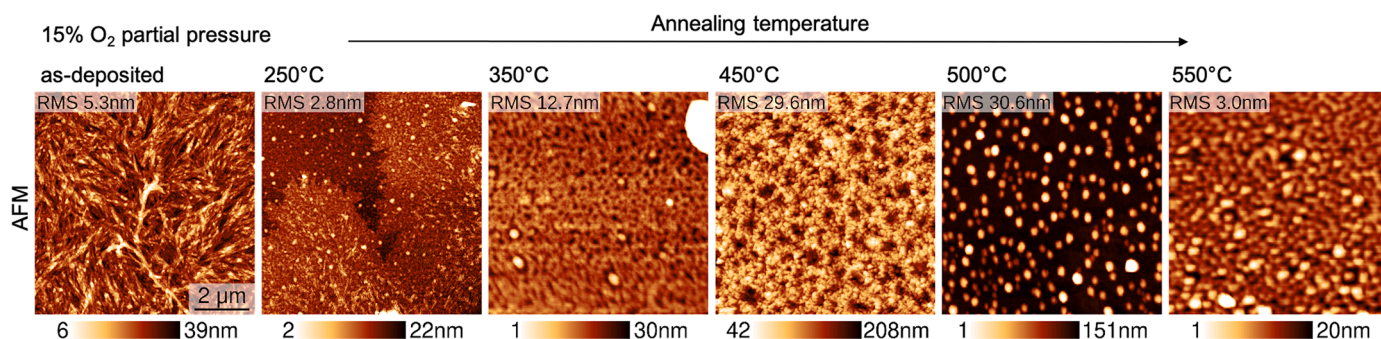


Fig. C.1. AFM topography of thin films sputtered on Si substrates at 15% O₂ partial pressure and annealed at different temperatures. The scanned area is 8 × 8 μm². The AFM images show an increase in the RMS roughness as the temperature increases only the sample at 550°C shows again a very smooth surface. In contrast to the 23% O₂ sample in Fig. 6, here the as-deposited and the 250°C samples show the presence of crystallites, discussed in section 3.4, because in this case AFM was performed several months after deposition.

vacuum annealing, thus we cannot rule out air contamination, and glove box annealing to remove residual water was not conducted. Generally, contamination by water homogenizes work function differences at surfaces, therefore, we do not expect to see theoretical values for the work functions of CuO and Cu₂O [76].

3.4. Investigation of aging effects

Finally, we investigated the aging effects on the RF-magnetron sputtered film by comparing AFM, KPFM and SEM images taken immediately after deposition (see Figs. 1 and 6) with those obtained after a several months aging period at room conditions. Fig. 8a shows AFM and KPFM images, and Fig. 8b SEM images, of aged, non-annealed samples deposited with 23% oxygen (21 months aging). Fig. 8c shows AFM and KPFM images and Fig. 8d SEM images of the sample deposited

with 15% oxygen (15 months aging). In the 15% samples, AFM and KPFM images show a dendritic morphology of the crystallites. These samples (as well as those annealed at 250°C, shown in Fig. C.1), present crystallites on the surface, which were not present immediately after deposition. This clearly indicates the instability of copper oxide when not subjected to high temperature vacuum annealing. The samples annealed at higher temperature did not show this crystallite growth, even 24 months after their deposition, hence the higher annealing temperatures help to enhance the stability of these films. This aging phenomenon cannot be attributed to a reduced oxygen level in the film in the deposition parameters, since it is occurring for both oxygen partial pressures. We recommend that more studies are conducted in this regard, as very limited literature is available on the aging of copper oxide and no existing studies have shown crystallite growth as a sign of copper oxide instability, despite its importance for the development of long-

standing photovoltaic devices.

4. Conclusions

In this work, we have grown copper oxide thin films at varying oxygen partial pressure (15 and 23%) and studied the effect of annealing in vacuum on the resulting films to study possible routes to yield pure phase cuprous oxide (Cu₂O). With increasing annealing temperature, we observe the formation of large grains and the presence of porosity. The thin films' structural properties were studied using Raman spectroscopy and X-ray diffraction; both techniques give consistent results, showing that the lower oxygen pressure at deposition favours the formation of Cu₂O. In the high oxygen partial pressure sample, annealing in vacuum favours the formation of Cu₂O, as CuO is reduced to Cu₂O when annealed at temperatures above the critical temperature of 350 °C. The Energy-dispersive X-ray spectroscopy composition analysis further supports the reduced oxygen content in these films. The homogeneity of the grown thin films was assessed using Raman mapping, as well as Kelvin Probe Force Microscopy (KPFM) measurements. Furthermore, KPFM measurements suggest that the CuO segregates and vanishes at annealing temperatures above 500 °C. Finally, we found that the pristine samples and those annealed at low temperatures displayed unwanted crystal growth when exposed to atmospheric conditions for a few months. Quite remarkably, annealing the samples prevented this unwanted growth. The Scanning Electron Microscopy and Atomic Force Microscopy prove the stability of the films annealed at temperatures equal or higher than 350 °C. Our work could aid in the reliable and reproducible production of high quality Cu₂O films for photovoltaic applications.

CRedit authorship contribution statement

Medina Umar: Validation, Formal analysis, Investigation, Writing – original draft, Visualization. **Milo Y. Swinkels:** Validation, Investigation, Writing – original draft. **Marta De Luca:** Methodology, Formal analysis, Investigation, Writing – original draft. **Claudia Fasolato:** Formal analysis, Investigation, Writing – review & editing. **Lucas Moser:** Methodology, Writing – review & editing. **Gerard Gadea:** Methodology, Formal analysis, Investigation, Writing – review & editing. **Laurent Marot:** Resources, Writing – review & editing. **Thilo Glatzel:** Conceptualization, Methodology, Writing – review & editing, Supervision, Project administration. **Iaria Zardo:** Methodology, Writing – review & editing, Supervision, Project administration, Funding acquisition.

Declaration of Competing Interest

The authors declare that they have no known competing financial interests or personal relationships that could have appeared to influence the work reported in this paper.

Acknowledgements

I.Z. acknowledges financial support from the European Research Council (ERC) under the European Union's Horizon 2020 research and innovation program (grant agreement No 756365). M.D.L. acknowledges support from the Swiss National Science Foundation Ambizione grant (Grant No. PZ00P2_179801). T.G. acknowledges financial support from the Swiss National Science Foundation (SNSF), the Swiss Nanoscience Institute (SNI) and the University of Basel. M.U. acknowledges fellowship funding from the Tertiary Education Trust Fund under AST&D University of Abuja and the Freiwillige Akademische Gesellschaft, Basel.

References

- [1] J. Bouclé, P. Ravirajan, J. Nelson, Hybrid polymer–metal oxide thin films for photovoltaic applications, *J. Mater. Chem.* 17 (2007) 3141–3153, <https://doi.org/10.1039/b706547g>.
- [2] R.A. José, M. Fernández-Gracia, (Eds), (2007), Synthesis, properties and application of oxide nanoparticles. Wiley: New Jersey. ISBN: 9780470108970. 10.1002/0470108975.
- [3] R. José, T. Velmurugan, R. Seeram, Metal oxides for dye-sensitized solar cells, *J. Am. Ceramic Soc.* 92 (2009) 289–301, <https://doi.org/10.1111/j.1551-2916.2008.02870.x>.
- [4] V.E. Henrich, P.A. Cox, Surface Chemistry of Metal Oxides, 464, Cambridge University Press, Cambridge, UK, 1994, pp. 91–94, <https://doi.org/10.1002/adma.19950070122>. XIVISBN: 052144389-X.
- [5] E. Fortunato, P. Barquinha, R. Martins, Oxide semiconductor thin film transistors: a review of recent advances, *Adv. Mater.* 24 (2012) 2945–2986, <https://doi.org/10.1002/adma.201103228>.
- [6] L. Petti, N. Münzenrieder, C. Vogt, H. Faber, L. Büthe, G. Cantarella, F. Bottacchi, T. D Anthopoulos, G. Tröster, Metal oxide semiconductor thin-film transistors for flexible electronics, *Appl. Phys. Rev.* 3 (2016), 021303, <https://doi.org/10.1063/1.4953034>.
- [7] E. Fortunato, D. Ginley, H. Hosono, D.C. Paine, Transparent conducting oxides for photovoltaics, *MRS Bull* (2007) 32242–32247, <https://doi.org/10.1557/mrs2007.29>.
- [8] S. Rühle, A.Y. Anderson, H.N. Barad, B. Kupfer, Y. Bouhadana, E. Rosh-Hodesh, Ariel Zaban, All-oxide photovoltaics, *J. Phys. Chem. Lett.* 3 (2012) 3755–3764, <https://doi.org/10.1021/jz3017039>.
- [9] B.D. Yuhas, P. Yang, Nanowire-based all-oxide solar cells, *J. Am. Chem. Soc.* 131 (3) (2009) 756–3761, <https://doi.org/10.1021/ja8095575>.
- [10] S. Nakano, N. Saito, K. Miura, T. Sakano, K. Ueda, K. Sugi, Highly reliable a-IGZO TFTs on plastic substrate for flexible AMOLED display, *J. Soc. Inf. Disp.* 20 (2012) 364–371, <https://doi.org/10.1002/jsid.111>.
- [11] S. Siol, C.J. Hellmann, S.D. Tilley, M. Grätzel, J. Morasch, J. Deuermeier, W. Jägermann, A. Klein, Band alignment engineering at Cu₂O/ZnO heterointerfaces, *ACS Appl. Mater. Interfaces* 8 (33) (2016) 21824–21831, <https://doi.org/10.1021/acsami.6b07325>.
- [12] M. Jahangir-Moghadam, K. Ahmadi-Majlan, X. Shen, T. Droubay, M. Bowden, M. Chrysler, D. Su, S.A. Chambers, J.H. Ngai, Band-gap engineering at a semiconductor-crystalline oxide interface, *Adv. Mater. Interfaces* 2 (4) (2015) 1–7, <https://doi.org/10.1002/admi.201400497>.
- [13] O. Lupan, V. Cretu, V. Postica, N. Ababii, O. Polonskyi, V. Kaidas, F. Schütt, Y. K. Mishra, E. Monaico, I. Tiginyanu, V. Sontea, T. Strunskus, F. Faupel, R. Adelung, Enhanced ethanol vapour sensing performances of copper oxide nanocrystals with mixed phases, *Sens. Actuators B* 224 (2016) 434–448, <https://doi.org/10.1016/j.snb.2015.10.042>.
- [14] L. Xu, H. Xu, S. Wu, X. Zhang, Synergy effect over electrodeposited submicron Cu₂O films in photocatalytic degradation of methylene blue, *Appl. Surf. Sci.* 258 (11) (2012) 4934–4938, <https://doi.org/10.1016/j.apsusc.2012.01.122>.
- [15] J. Dong, H. Xu, F. Zhang, C. Chen, L. Liu, G. Wu, Synergistic effect over photocatalytic active Cu₂O thin films and their morphological and orientational transformation under visible light irradiation, *Appl. Catal. A* 470 (2014) 294–302, <https://doi.org/10.1016/j.apcata.2013.11.010>.
- [16] A.E. Rakshani, Preparation Characterization and photovoltaic properties of cuprous oxide – a review, *Solid State Electronics* 29 (1) (1986) 7–17, [https://doi.org/10.1016/0038-1101\(86\)90191-7](https://doi.org/10.1016/0038-1101(86)90191-7).
- [17] A.C. Zivković, A. Roldan, N.H. de Leeuw Density functional theory study explaining the underperformance of copper oxides as photovoltaic absorbers, *Phys. Rev. B* 99 (2019), 035154, <https://doi.org/10.1103/PhysRevB.99.035154>.
- [18] A.S. Zoofakar, R.A. Rani, A.J. Morfa, A.P. O'Mullane, K. Kalantar-zadeh, Nanostructured copper oxide semiconductors: a perspective on materials, synthesis methods and applications, *State J. Mat. Chem. C* 27 (2) (2014) 5247–5270, <https://doi.org/10.1039/C4TC00345D>.
- [19] R.K. Swarnkar, S.C. Singh, R. Gopal, Synthesis of copper/copper-oxide nanoparticles: optical and structural characterizations, in: AIP Conference Proceedings 1147, 2009, p. 205, <https://doi.org/10.1063/1.3183432>.
- [20] W.L. Yu, Y.Z. Lin, X.W. Zhu, Z.G. Hu, M.J. Han, S.S. Cai, L.L. Chen, H.H. Shao, Diversity of electronic transitions and photoluminescence properties of p-type cuprous oxide films: a temperature-dependent spectral transmittance study, *J. Appl. Phys.* 117 (2015), 045701, <https://doi.org/10.1063/1.4906405>.
- [21] B.K. Meyer, A. Polity, D. Reppin, M. Becker, P. Hering, P.J. Klar, T. Sander, C. Reindl, J. Benz, M. Eickhoff, C. Heiliger, M. Heinemann, J. Bläsing, A. Krost, S. Shokovets, C. Müller, C. Ronning, Binary copper oxide semiconductors: From material toward devices, *Phys. Status Solidi B* 249 (2012) 1487, <https://doi.org/10.1002/pssb.201248128>.
- [22] W. Zheng, Y. Chen, X. Peng, K. Zhong, Y. Lin, Z. Huang, The phase evolution and physical properties of binary copper oxide thin films prepared by reactive magnetron sputtering, *Materials* 11 (2018) 1253.
- [23] K. Self, W. Zhou, Surface charge driven growth of eight-branched Cu₂O crystals X Cryst, *Growth Des* 16 (2016) 5377–5538, <https://doi.org/10.1021/acs.cgd.6b00883>.
- [24] V. Figueiredo, E. Elangovan, G. Goncalves, P. Barquinha, L. Pereira, N. Franco, E. Alves, R. Martins, E. Fortunato, Effect of post-annealing on the properties of copper oxide thin films obtained from the oxidation of evaporated metallic copper, *Appl. Surf. Sci.* 254 (2007) 3949–3954, <https://doi.org/10.1016/j.apsusc.2007.12.019>.

- [25] S.C. Ray, Preparation of copper oxide thin film by the sol-gel like dip technique and study of their structural and optical properties, *Sol. Energy Mater. Sol. Cells* 68 (2001) 307–312, [https://doi.org/10.1016/S0927-0248\(00\)00364-0](https://doi.org/10.1016/S0927-0248(00)00364-0).
- [26] G. Papadimitropoulos, N. Vourdas, V.E. Vamvakas, D. Davazoglou, Deposition and characterization of copper oxide thin films, *Journal of Physics: Conference Series* 10 (2005) 182–185, <https://doi.org/10.1088/1742-6596/10/1/045>.
- [27] A. Thobor, J.F. Pierson, Properties and air annealing of paramelaconite thin films, *Materials Letters* 57 (2003) 3676–3680, [https://doi.org/10.1016/S0167-577X\(03\)00148-4](https://doi.org/10.1016/S0167-577X(03)00148-4).
- [28] K. Santra, C.K. Sarker, M.K. Mukherjee, B. Ghosh, Copper oxide thin films grown by plasma evaporation method, *Thin Solid Films* 213 (1992) 226–229, [https://doi.org/10.1016/0040-6090\(92\)90286-K](https://doi.org/10.1016/0040-6090(92)90286-K).
- [29] T. Maruyama, Copper oxide thin films prepared by chemical vapor deposition from copper dipivaloylmethanate, *Sol. Energy Mater. Sol. Cells* 56 (1998) 85–92, [https://doi.org/10.1016/S0927-0248\(98\)00128-7](https://doi.org/10.1016/S0927-0248(98)00128-7).
- [30] E. Carbó-Argibay, X-Q. Bao, C. Rodríguez-Abreu, M.F. Cerqueira, D.Y. Petrovykh, L. Liu, Y.V. Kolen'ko, Up-scaling the synthesis of Cu₂O submicron particles with controlled morphologies for solar H₂ evolution from water, *J. Colloid Interface Sci.* 456 (2015) 219, <https://doi.org/10.1016/j.jcis.2015.06.014>.
- [31] N. Serin, T. Serin, S. Horzum, Y. Celik, Annealing effects on the properties of copper oxide thin films prepared by chemical deposition, *Semicond. Sci. Technol.* 20 (2005) 398–401, <https://doi.org/10.1088/0268-1242/20/5/012>.
- [32] M.D. Susman, Y. Feldman, A. Vaskevich, I. Rubinstein, Chemical deposition of Cu₂O Nanocrystals with precise morphology control, *ACS Nano* 8 (2014) 162, <https://doi.org/10.1021/nn405891g>.
- [33] V. Figueiredo, J.V. Pinto, J. Deuermeier, R. Barros, E. Alves, R. Martins, P-Type Cu_xO thin-film transistors produced by the thermal oxidation, *J. Disp. Technol.* 9 (2013) 735–740, <https://doi.org/10.1109/JDT.2013.2247025>.
- [34] L.C.-K. Liau, Y.-C. Lin, Y.-J. Peng, Fabrication pathways of p-n Cu₂O homojunction films by electrochemical deposition processing, *J. Phys. Chem. C* 117 (2013) 26426, <https://doi.org/10.1021/jp405715c>.
- [35] K.H. Yoon, W.J. Choi, D.H. Kang, Photoelectrochemical properties of copper oxide thin films coated on an n-Si substrate, *Thin Solid Films* 372 (2000) 250–256, [https://doi.org/10.1016/S0040-6090\(00\)01058-0](https://doi.org/10.1016/S0040-6090(00)01058-0).
- [36] Z. Li, K. Tong, R. Shi, Y. Shen, Y. Zhang, Z. Yao, J. Fan, M. Thwaites, G. Shaoa, Reactive plasma deposition of high quality single phase CuO thin films suitable for metal oxide solar cells, *J. Alloy Metal* 695 (2017) 3116–3123, <https://doi.org/10.1016/j.jallcom.2016.11.338>.
- [37] J.F. Pierson, A. Thobor-Keck, A. Billard, Cuprite paramelaconite and tenorite films deposited by reactive magnetron sputtering, *Appl. Surf. Sci.* 210 (2003) 359–367, [https://doi.org/10.1016/S0169-4332\(03\)00108-9](https://doi.org/10.1016/S0169-4332(03)00108-9).
- [38] A.A. Ogwu, T.H. Darma, A reactive magnetron sputtering route for attaining a controlled core rim phase partitioning in Cu₂O/CuO thin films with resistive switching potential, *J. Appl. Phys.* 113 (2013), 183522, <https://doi.org/10.1063/1.4804326>.
- [39] J. Hsieh, P. Kuo, K. Peng, S. Liu, J. Hsueh, S. Chang, Opto-electronic properties of sputter-deposited Cu₂O films treated with rapid thermal annealing, *Thin Solid Films* 516 (16) (2008) 5449–5453, <https://doi.org/10.1016/j.tsf.2007.07.097>.
- [40] J. Sohn, S.-H. Song, D.-W. Nam, I.-T. Cho, E.-S. Cho, J.-H. Lee, **Effects of vacuum annealing on the optical and electrical properties of p-type copper-oxide thin-film transistors**, *Semicond. Sci. Technol.* 28 (2013), 015005, <https://doi.org/10.1088/0268-1242/28/1/015005>.
- [41] M.S. Abbas, M.A. Mahdi, Z. Hassan, Fabrication of Cu₂O nanocrystalline thin films photosensor prepared by RF sputtering technique, *Physical E* 94 (2017) 132–138, <https://doi.org/10.1016/j.physe.2017.08.007>.
- [42] R.-S. Yu, Y.-C. Lee, Effects of annealing on the optical and electrical properties of sputter-deposited CuGaO₂, *Thin Solid Films* 646 (2018) 143–149, <https://doi.org/10.1016/j.tsf.2017.11.026>.
- [43] J. Ramirez-Ortiz, T. Ogura, J. Medina-Valtierra, S.E. Acosta-Ortiz, P. Bosch, J.A. de los Reyes Lara, A catalytic application of Cu₂O and CuO films deposited over fiberglass, *Appl. Surf. Sci.* 174 (2001) 177–184, [https://doi.org/10.1016/S0169-4332\(00\)00822-9](https://doi.org/10.1016/S0169-4332(00)00822-9).
- [44] C.L. Azanza Ricardo, M. D'Incau, M. Leoni, C. Malerba, A. Mittiga, P. Scardi, Structural properties of RF-magnetron sputtered Cu₂O thin films, *Thin Solid Films* 520 (2011) 280–286, <https://doi.org/10.1016/j.tsf.2011.07.066>.
- [45] S.S. Guru Srinivasan, B. Govardhanan, P. Aabel, M. Ashok, M.C. Santhosh Kumar, Effect of oxygen partial pressure on the tuning of copper oxide thin films by reactive sputtering solar light driven photocatalysis, *Solar Energy* 187 (2019) 368–378, <https://doi.org/10.1016/j.solener.2019.05.057>.
- [46] V.S. Levitskii, V.I. Shapovalov, A.E. Komlev, E.S. Shutova, Raman spectroscopy of copper oxide films deposited by reactive magnetron sputtering, *Technical Physics Letters* 41 (11) (2015) 1094–1096, <https://doi.org/10.1134/S106378501511022X>.
- [47] P. Pattanasattayavong, S. Thomas, G. Adamopoulos, M.A. McLachlan, T. D. Anthopoulos, P-channel thin-film transistors based on spray-coated Cu₂O films, *Appl. Phys. Lett.* 102 (16) (2013), 163505, <https://doi.org/10.1063/1.4803085>.
- [48] B. Purusottam-Reddy, K. Sivajee-Ganesh, K. Jayanth-Babu, O. Hussain, C. Julien, Microstructure and super capacitive properties of RF-sputtered copper oxide thin films: influence of O₂/Ar ratio, *Ionics* 21 (8) (2015) 2319–2328, <https://doi.org/10.1007/s11581-015-1403-5>.
- [49] A. Rydosz, Amorphous and nanocrystalline magnetron sputtered CuO thin films deposited on low temperature cofired ceramics substrates for gas sensor applications, *Sensors J* 14 (2014) 1600–1607, <https://doi.org/10.1109/JSEN.2014.2301031>.
- [50] Z.Q. Yao, S.L. Liu, L. Zhang, B. He, A. Kumar, X. Jiang, Room temperature fabrication of p-channel Cu₂O thin-film transistors on flexible polyethylene terephthalate substrates, *Appl. Phys. Lett.* 101 (2012), 042114, <https://doi.org/10.1063/1.4739524>.
- [51] S. Shyamal, P. Hajra, H. Mandal, J.K. Singh, A.K. Satpati, S. Pande, C. Bhattacharya, Effect of substrates on the photoelectrochemical reduction of water over cathodically electrodeposited p-type Cu₂O thin films, *ACS Appl. Mater. Interfaces* 7 (33) (2015) 18344–18352, <https://doi.org/10.1021/acsami.5b04116>.
- [52] E. Camacho-Espinosa, I. Rimmaudo, I. Reich, R. Mis-Fernández, J.L. Peña, Stability of sputter deposited cuprous oxide (Cu₂O) subjected to ageing conditions for photovoltaic application, *J. Appl. Phys.* 123 (2018), 085301, <https://doi.org/10.1063/1.5017538>.
- [53] M. Heinemann, B. Eifert, C. Heiliger, Band structure and phase stability of the copper oxides Cu₂O, CuO, and Cu₄O₃, *Phys. Rev. B* 87 (2013), 115111, <https://doi.org/10.1103/PhysRevB.87.115111>.
- [54] J.H. Hsieh, P.W. Kuo, K.C. Peng, S.J. Liu, J.D. Hsueh, S.C. Chang, Opto-electronic properties of sputter-deposited Cu₂O films treated with rapid thermal annealing, *Thin Solid Films* 516 (16) (2008) 5449–5453, <https://doi.org/10.1016/j.tsf.2007.07.097>.
- [55] L. Guo, M. Zhao, D.-M. Zhuang, M. Cao, L. Ouyang, X. Li, R. Sun, Z. Gao, Influences of CuO phase on electrical and optical performance of Cu₂O films prepared by middle frequency magnetron sputtering, *Appl. Surf. Sci.* 359 (2015) 36–40, <https://doi.org/10.1016/j.apsusc.2015.09.216>.
- [56] J. Sohn, S.-H. Song, D.-W. Nam, I.-T. Cho, E.-S. Cho, J.-H. Lee, K. H.-In, Effects of vacuum annealing on the optical and electrical properties of p-type copper-oxide thin-film transistors, *Semicond. Sci. Technol.* 28 (2013), 015005, <https://doi.org/10.1088/0268-1242/28/1/015005>.
- [57] S.I. Santhosh, L. Marot, B. Eren, R. Steiner, L. Moser, D. Mathys, M. Düggelin, P. Chapon, E. Meyer, Morphological changes of tungsten surfaces by low-flux helium plasma treatment and helium incorporation via magnetron sputtering, *ACS Appl. Mat. & Int.* 6 (14) (2014) 11609–11616, <https://doi.org/10.1021/am502370t>.
- [58] S. Sadewasser, T. Glatzel, Experimental technique and working modes, in: S. Sadewasser, T. Glatzel (Eds.), *Experimental technique and working modes, Kelvin Probe Force Microscopy*. Springer Series in Surface Sciences, 65, Springer International Publishing, Cham, 2018. www.springer.com/gp/book/9783319756868.
- [59] Ch. Sommerhalter, Th.W. Matthes, Th. Glatzel, A. Jäger-Waldau, M.Ch. Lux-Steiner, High-sensitivity quantitative Kelvin probe microscopy by noncontact ultra-high-vacuum atomic force microscopy, *Appl. Phys. Lett.* 75 (1999) 286, <https://doi.org/10.1063/1.1243>.
- [60] M.T.S. Nair, L. Guerrero, O.L. Arenas, P.K. Nair, Chemically deposited copper oxide thin films: structural, optical and electrical characteristics, *Appl. Surf. Sci.* 150 (1999) 143–151. PII: S0169-4332(99)00239-1.
- [61] P.S. Murphin Kumar, H.H. Kyaw, M.T.Z. Myint, L. Al-Haj, A. Al-Muhtaseb, M. Al-Abri, V. Thanigaivel, V.K. Ponnusamy, Green route synthesis of nanoporous copper oxide for efficient supercapacitor and capacitive deionization performances, *Int. J. Energy Res.* 44 (2020) 13, <https://doi.org/10.1002/er.5712>.
- [62] R. Messier, Toward quantification of thin films morphology, *J. Vacuum Sci. Technol. A* 490 (4) (1986), <https://doi.org/10.1116/1.573866>.
- [63] C. Straub, L. Wegewitz, S. Schöler, U. Holländer, K. Möhwald, W. Maus-Friedrichs, Surface deoxidation mechanism during vacuum heat treatment of stainless steels AISI 304 and 446, *Steel Res. Int.* 91 (2020), 1900568, <https://doi.org/10.1002/srin.201900568>.
- [64] A. Guillén-Cervantes, Z. Rivera-Alvarez, M. López-López, E. López-Luna, I. Hernández-Calderón, GaAs surface oxide desorption by annealing in ultra high vacuum, *Thin Solid Films* 373 (2000) 159, [https://doi.org/10.1016/S0040-6090\(00\)01126-3](https://doi.org/10.1016/S0040-6090(00)01126-3).
- [65] O. Messaoudi, H. Makhlof, A. Souissi, I.B. Assaker, G. Amiri, A. Bardaoui, M. Oueslati, M. Bechelany, R. Chtourou, Synthesis and characterization of ZnO/Cu₂O core-shell nanowires grown by two-step electrodeposition method, *Appl. Surf. Sci.* 343 (2015) 148–152, <https://doi.org/10.1016/j.apsusc.2015.03.045>.
- [66] Y. Wang, J. Ghanbaja, F. Soldera, S. Migot, P. Boulet, D. Horwat, F. Mücklich, J.-F. Pierson, Tuning the structure and preferred orientation in reactively sputtered copper oxide thin film, *Appl. Surf. Sci.* 335 (2015) 85–91, <https://doi.org/10.1016/j.apsusc.2015.02.028>.
- [67] Y.P. Yu, Y.R. Shen, Y. Petroff, L.M. Falicov, Resonance dipole-Raman scattering at the forbidden yellow exciton in Cu₂O, *Phys. Rev. Lett.* 30 (1973) 283, <https://doi.org/10.1103/PhysRevLett.30.283>.
- [68] Y.P. Yu, Y.R. Shen, Resonance Raman studies in Cu₂O. I. The phonon-assisted 1s yellow excitonic absorption edge, *Phys. Rev. B* 12 (1975) 1377, <https://doi.org/10.1103/PhysRevB.12.1377>.
- [69] D. Cakir, **Enhanced Raman signatures on copper based-materials**, Ph.D. Thesis, Université Montpellier, 2017.
- [70] D. Powell, A. Compaan, J.R. Macdonald, Raman-scattering study of ion-implantation-produced damage in Cu₂O, *Phys. Rev. B* 12 (1975) 20, <https://doi.org/10.1103/PhysRevB.12.20>.
- [71] J. Chrzanowski, J.C. Irwin, Raman scattering from cupric oxide, *Solid State Commun.* 70 (1) (1989) 11–14, [https://doi.org/10.1016/0038-1098\(89\)90457-2](https://doi.org/10.1016/0038-1098(89)90457-2).
- [72] N.A. Mohammed Shanid, M. Abdul Khadar, V.G. Sathe, Frohlich interaction and associated resonance enhancement in nanostructured copper oxide films, *J. Raman Spectrosc.* 42 (2011) 1769–1773, <https://doi.org/10.1002/jrs.2945>.
- [73] H. Solache-Carranco, G. Juárez-Díaz, A. Esparza-García, M. Briseño-García, M. Galván-Arellano, J. Martínez-Juárez, G. Romero-Paredes, R. Peña-Sierra, Photoluminescence and X-ray diffraction studies on Cu₂O, *Journal of Luminescence* 129 (2009) 1483–1487, <https://doi.org/10.1016/j.jlumin.2009.02.033>.

- [74] Z.H. Gan, G.Q. Yu, B.K. Tay, C.M. Tan, Z.W. Zhao, Y.Q. Fu, Y. Q., Preparation and characterization of copper oxide thin films deposited by filtered cathodic vacuum arc, *J. Phys. D: Appl. Phys.* 37 (2004) 81–85. PII: S0022-3727(04)69209-6.
- [75] F.A. Akgul, G. Akgul, N. Yildirim, H.E. Unalan, R. Turan, Influence of thermal annealing on microstructural, morphological, optical properties and surface electronic structure of copper oxide thin film, *Mater. Chem. Phys.* 147 (2014) 987–995, <https://doi.org/10.1016/j.matchemphys.2014.06.047>.
- [76] B. Singh, B.R. Mehta, Relationship between nature of metal-oxide contacts and resistive switching properties of copper oxide thin film based devices, *Thin Solid Films* 569 (2014) 35–43, <https://doi.org/10.1002/pssb.201248128>.
- [77] S. Sadewasser and T. Glatzel, Experimental technique and working modes, In: *Kelvin Probe Force Microscopy: From Single Charge Detection to Device Characterization*, S. Sadewasser, T. Glatzel, Eds., Springer Series in Surface Sciences; Springer Berlin Heidelberg: Berlin, Heidelberg, 2018; Vol. 65, pp. 3-22. www.springer.com/gp/book/9783319756868.